DRAFT VERSION MAY 6, 2013
Preprint typeset using LaTeX style emulateapj v. 12/01/06

DATA PAPER

JESSICA L. EVANS,[1] CHRISTOPHER W. CHURCHILL,[1] MICHAEL T. MURPHY,[2], AND NIKOLE M. NIELSEN[1]

Draft version May 6, 2013

ABSTRACT

Subject headings: quasars: absorption lines

1. INTRODUCTION

Our current understanding of galaxy formation and evolution is still far from complete. Quasar absorption line systems are an extremely useful means of statistically constraining scenarios of metal enrichment, inflow and outflow, ionization conditions, kinematics, and gas structure within galaxies and the IGM.

For the following discussion, we adopt the terms "weak" and "strong" to refer to absorbers having 0.02 Å $\leq W_r < 0.3$ Å and $W_r \geq 0.3$ Å, respectively, where W_r is the rest frame equivalent width of the Mg II λ2796 transition.

Numerous studies have identified specific galaxies associated with Mg II absorption (see Bergeron & Boissè 1991; Steidel, Dickinson, & Persson 1994; Steidel et al. 1997; Guillemin & Bergeron 1997; Churchill et al. 2005; Chen & Tinker 2008; Kacprzak et al. 2008; Barton & Cooke 2009; Chen et al. 2010; Kacprzak et al. 2011; Churchill et al. 2012; Nielsen et al. 2012), while weak absorption is believed to be generally associated with the IGM or CGM (Churchill et al. 1999; Rigby et al. 2002; Nielsen et al. 2012).

In this paper we present the largest study of high resolution, high signal-to-noise Mg II absorption to date, with an emphasis on kinematics and evolution. The redshift path density of weak Mg II absorption and its dependence on quasar luminosity were explored in Evans et al. (2012); in this paper the entire Mg II absorber sample and results for equivalent width and kinematic quantities are presented. Our Voigt Profile (VP) modeling and results will be discussed in Paper II.

In § 2 we present our data, and in § 3 our results for equivalent widths, kinematic extents, kinematic systems, and flux decrements as a function of velocity, as well as how these properties have evolved. We discuss plausible interpretations in § 4, and conclude in § 5.

2. DATA

2.1. *Spectra*

We have analyzed 252 high resolution, high signal-to-noise High Resolution Echelle Spectrometer (HIRES) and Ultraviolet and Visual Echelle Spectrograph (UVES) quasar spectra obtained from the Keck and Very Large Telescope (VLT) observatories, respectively. The wavelength coverage of the spectra is approximately 3,000 - 10,000 Å. An example spectrum is shown in Figure 1. The resolving power of both instruments is $R = \lambda/\Delta\lambda = 45,000$, or ~ 6.6 km s^{-1}, and the spectra have three pixels per resolution element. The resolution is constant in velocity. The signal-to-noise ratios are typically 25 - 80. Such high quality spectra allow for an in-depth investigation into the distributions and kinematics of the galactic halos and intergalactic structures selected by the presence of the Mg II $\lambda\lambda$2796, 2803 doublet. The high resolution allows us to discern fine substructure within the absorption features.

TABLE 1
JOURNAL OF OBSERVATIONS

Quasar[a]	Alias	z_{em}	λ_{blue} (Å)	λ_{red} (Å)	Facility
J000323–260318	Q0000–263	4.111	5122	8143	1
J000149–015939	UM196	2.817	3045	10087	1, 2
J000520+052411	UM18	1.900	3188	6081	1
J000344–232355	HE0001–2340	2.280	3044	10088	2
J000448–415728	Q0002–422	2.760	3044	10087	2

Notes. Table 1 is published in its entirety in the electronic edition of the Journal. A portion is shown here for guidance regarding its form and content.

[a] Quasar names are as listed in Veron-Cetty & Veron (2001).

Facilities. (1) HIRES; (2) UVES.

The HIRES spectra were provided by Charles Steidel, Jason Prochaska, Christopher Churchill, Wallace Sargent, and Michael Rauch. The UVES spectra were provided by the UVES Squad, an international collaboration headed by Michael Murphy that mines UVES archived quasar spectra. The spectra of Churchill and Steidel were explicitly observed for Mg II absorption (Churchill & Vogt 2001; Churchill et al. 2003; Steidel et al. 2002) and were selected based upon previous studies which used low resolution spectra to detect Mg II absorption of equivalent widths $W_r(2796) \geq 0.3$ Å (Sargent et al. 1988; Steidel & Sargent 1992). Those of Sargent and Rauch were selected for high resolution analysis of Lyα forest and C IV absorption, and those of Prochaska for damped Lyman alpha (DLA) absorption (Prochaska et al. 2007). The UVES Squad spectra were drawn from the UVES/VLT archive by Michael Murphy. These spectra were obtained by several researchers for various purposes, including Lyα forest, Mg II, C IV, O IV, and DLA studies. The heterogeneous selection bias of our sample is addressed in § 2.7.

Examples of the spectra used in this study are listed in Table 1. For each quasar, column (1) lists the name we have adopted, (2) a common alias, (3) the emission redshift, (4) the lower wavelength limit observed, (5) the upper wavelength limit observed, and (6) the instrument with which the spectrum was obtained.

2.2. *Reduction*

The spectra of Churchill were reduced using the standard Image Reduction and Analysis Facility (IRAF[3]) software, the process of which is detailed in Churchill (1997). Those of Sargent, Rauch, Prochaska, and Steidel were reduced using

[1] New Mexico State University, Las Cruces, NM 88003

[2] Centre for Astrophysics and Supercomputing, Swinburne University of Technology, Hawthorn, Melbourne, VIC 3122, Australia

[3] IRAF is distributed by the National Optical Astronomy Observatories, which are operated by the Association of Universities for Research in Astronomy, Inc., under cooperative agreement with the National Science Foundation.

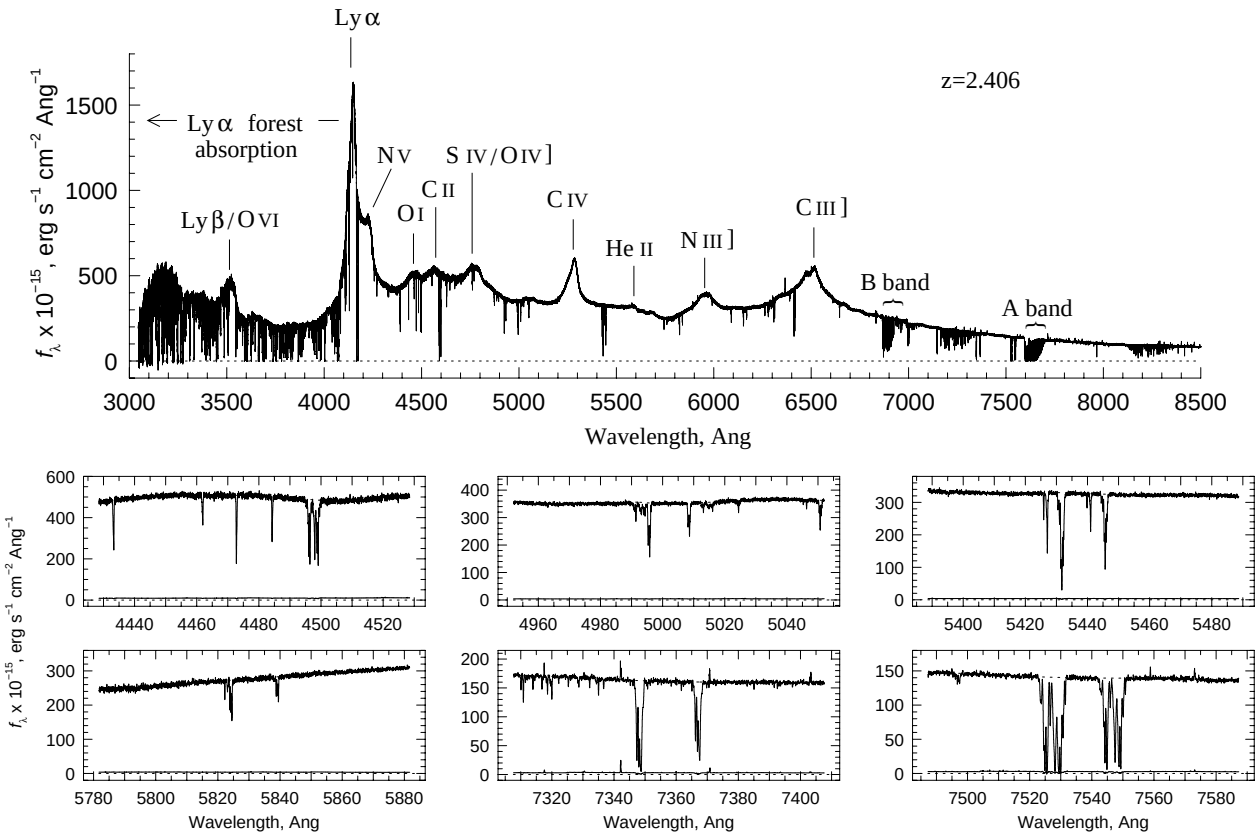

FIG. 1.— The UVES spectrum J222006–280323 and six of its Mg II systems presented in order of their absorption redshifts: 0.599508, 0.786512, 0.942415, 1.082795, 1.555851, and 1.692150.

the Mauna Kea Echelle Extraction (MAKEE) data reduction package of Barlow (2005), which is optimized for the spectral extraction of single, unresolved point sources. All of the HIRES spectra were previously continuum fit.

The UVES Squad spectra were reduced using the UVES pipeline (Dekker et al. 2000), which is provided by the European Southern Observatory (ESO). The pipeline runs in the ECHELLE context of the MIDAS environment. The echellogram layout is assessed using two calibration exposures, a quartz lamp and a short thorium-argon (ThAr) lamp. These are taken with a short slit so as to define a nominal trace along which the object spectrum will be extracted, as well as to provide an initial wavelength solution. The trace is refined by analyzing the quasar exposure, but the nominal trace provides a reasonable approximation in heavily absorbed regions of the spectrum. The wavelength solution is refined using a standard ThAr lamp exposure. Several hundred strong, unblended ThAr lines are used to constrain a two dimensional wavelength space model of the CCD. The wavelength calibration residuals for each order averaged 70 m/s, or about 0.03 pixels in a the final combined spectrum. Finally, the quasar flux is extracted and the ThAr wavelength calibration polynomial for each order is attached. During extraction, the blaze function is removed from the data by dividing the normalized flat fields into the object spectra. This ensures that extracted echelle orders which overlap in wavelength space have a similar continuum shape, allowing simple combination.

Some, but not all, of the exposures were then combined into one dimensional spectra using the UVES POst-Pipeline Echelle Reduction (UVES POPLER) software (Murphy 2008), which is an extra reduction step that facilitates cosmic ray removal. A sliding window is passed along each echelle order and the flux variance within the window is used to identify strong cosmic rays. The echelle orders in each exposure are scaled to a common flux level where they overlap, and the wavelength scales are corrected to the vacuum heliocentric frame. The data are then median filtered and combined using inverse variance weighting. An initial continuum is derived by iteratively fitting small sections of each spectrum with a low order Chebyshev polynomial, rejecting points lying many sigma below or above the fit at each iteration. The sections of continuum are then spliced together by linearly weighting each section from unity at their centers to zero at their edges. Any remaining artifacts, such as from internal spectrograph reflections, are removed and the continuum is refined manually. All manual actions are logged and the entire reduction and combination process is readily repeatable.

All the spectra in our sample have been corrected to heliocentric vacuum velocities. In cases where multiple spectra of a quasar were available, we optimally combined them in order to increase wavelength coverage and signal-to-noise ratio.

2.3. *Characteristics of the Spectra*

The Mg II λ2796 redshift coverage of the survey is $0.1 < z < 2.6$ and is illustrated in Figure 2.1. The thin lines indicate total coverage toward each quasar line of sight, while the thick lines indicate those regions of the spectra for which the 6 σ rest limiting equivalent width limit $W_{r,lim}$ is no greater than

0.02 Å. This quantity, discussed further in § 2.6, traces the sensitivity of spectra in each pixel, and in turn allows us to determine what range of equivalent widths are detectable in a given portion of a spectrum. Small gaps in the spectra are possible above $\sim$ 5000 Å due to incomplete coverage of the echelle orders by the CCDs.

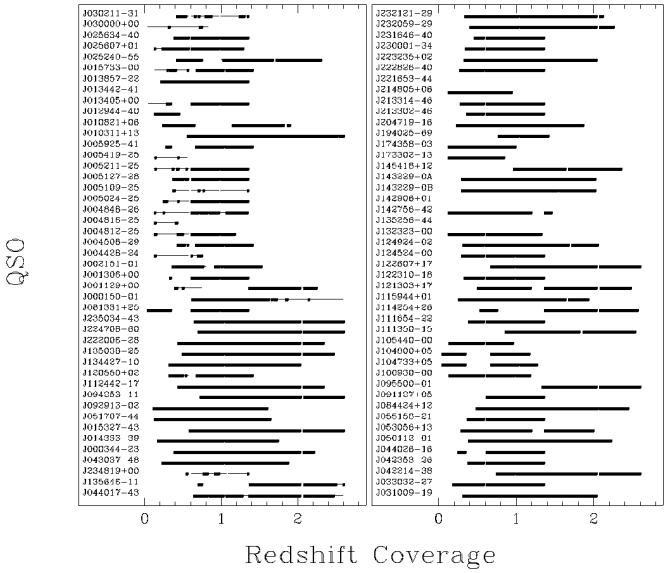

FIG. 2.1.— Examples of the redshift coverage of the quasar spectra in our sample. The thin lines indicate all coverage, while the thick lines indicate those regions of the spectra for which the 6 σ rest limiting equivalent width limit $W_{r,lim}$ is no greater than 0.02 Å. Figures 2.1–2.3 show the coverage for our full sample and are available in the online version of the Journal.

We also calculated the redshift path sensitivity function $g(W_r,z)$ of the survey (Lanzetta et al. 1987). This function represents the number of absorbers of a given rest equivalent width at a given redshift that could have been detected in the sample. The maximum possible value of $g(W_r,z)$ is equal to the total number of lines of sight. The redshift path sensitivity of our survey is shown in Figure 3. Note that the $g(W_r,z)$ function rises quickly with increasing equivalent width and thereafter is limited chiefly by the number of lines of sight that cover a given redshift, with the sensitivity peaking at $z \sim 1$.

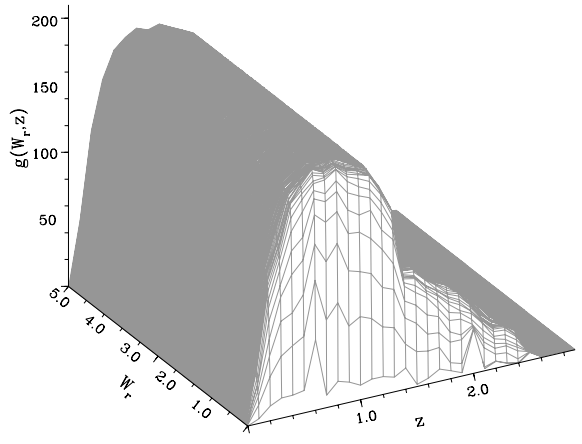

FIG. 3.— The redshift path sensitivity $g(W_r,z)$ of the survey.

2.4. *Identifying* Mg II *Doublets*

We searched quasar spectra only in the region spanning the Lyα emission redshift up to 5,000 km s^{-1} blueward of the Mg II emission redshift. This upper limit ensures that no detected Mg II absorption features are intrinsic to the quasar and its immediate vicinity (Weymann et al. 1991). Using the program SEARCH (Churchill et al. 1999), the spectra are objectively searched for Mg II doublet candidates. The initial criteria are the detection of a 5 σ feature, which is taken to be the λ2796 line, along with a corresponding 3 σ detection at what would be the location of the λ2803 feature. Detections and significance levels follow the formalism of Schneider et al. (1993). The candidates are then checked for doublet ratios consistent with $1.0 \leq DR \leq 2.0$. Finally, line profiles are visually inspected to ensure that they are consistent with each other and to eliminate any spurious features.

Two or more Mg II features are considered to be kinematic subsystems within a single system if they lie within 800 km s^{-1} of each other. The candidates are also checked automatically for corresponding absorption in numerous other atomic transitions, including Mg I λ2853; Fe II λ2344, λ2374, λ2383, λ2587, and λ2600; Ca II λ3935 and λ3970; and Mn II λ2577, λ2594, and λ2606. Using this algorithm, 469 Mg II $\lambda\lambda 2796, 2803$ systems were identified. However, after eliminating systems which were identified as Mg II doublets but which failed to meet a minimum standard of data quality (see § 2.6), 422 systems remained to comprise our sample.

2.5. *Problems at High Redshift*

Within the higher wavelength regimes of our sample (above $\sim$ 5900 Å), corresponding to higher Mg II λ2796 absorption redshifts, feature detection becomes more difficult due to the presence of telluric lines. The strongest lines occur in the A- and B-bands (7600–7630 and 6860–6890 Å, respectively) and also between 7170–7350 Å (Barlow 2005). These lines are generally distinguishable from the Mg II $\lambda\lambda 2796, 2803$ doublet. A chance alignment of two telluric lines at the precise separation needed, along with the required doublet ratio needed to be mistaken for the Mg II $\lambda\lambda 2796, 2803$ doublet, is unlikely; furthermore, the A- and B-band features in particular occur in a distinctive pattern of closely spaced pairs that is readily recognizable. Nevertheless, these spurious features may obscure underlying weak Mg II absorption or cause significant line blending. The search algorithm, however, is such that the redshifted Mg II λ2803 wavelength corresponding to a candidate Mg II λ2796 feature is always visually inspected, in addition to our objective criteria, to determine whether absorption is present. The locations of the Mg I, Fe II, Ca II, and Mn II features mentioned in § 2.4 are also visually inspected for possible corroboration of the presence of the Mg II $\lambda\lambda 2796, 2803$ doublet. These procedures ensure that the maximum possible number of absorbing systems are recovered from the spectra.

2.6. *Global Absorption Line Characteristics*

Figure 4 shows the binned redshift distributions of our detected Mg II $\lambda\lambda 2796, 2803$ absorbing systems for weak systems, strong systems, and the full equivalent width sample spanning $0.006 \leq W_r(2796) \leq 6.23$ Å. The absorbing redshifts span the range $0.19 \leq z \leq 2.55$, with a mean of 1.18. The more sharply declining tail at the high end of the weak population versus the strong is due partially to a decline in the sensitivity of the spectra in the higher redshift regime, as can be

seen in the illustration of the redshift path sensitivity (Figure 3); the lowest W_r systems suffer the most loss of completeness. The other reason behind the discrepancy is that there are truly fewer weak absorbers per unit redshift at high redshift than there are strong absorbers (see Evans et al. 2012, and references therein).

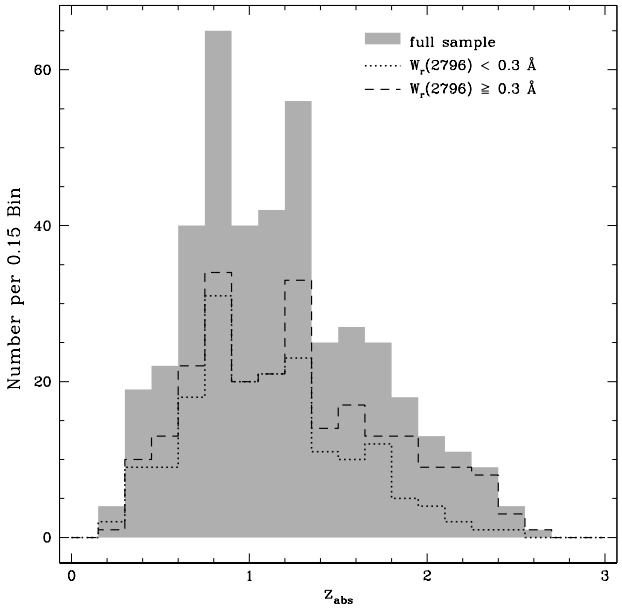

FIG. 4.— The Mg II absorption redshifts. The solid gray area indicates the full sample. The dotted and dashed lines indicate the weak and strong samples, respectively.

An average equivalent width limit over the Mg II λ2796 feature consistent with $W_{r,lim} \leq 0.02$ Å was a prerequisite for inclusion in our final sample. This quantity is defined as the minimum rest equivalent width detectable in a given portion of a spectrum, and is a measure of the signal-to-noise ratio. In this case, the mean 6 σ $W_{r,lim}$ was calculated over $\pm$600 km s^{-1} about the λ2796 feature. Systems were included for which (1) $W_{r,lim} \leq 0.02$ Å; *or* (2) for which $W_{r,lim}$ was greater than 0.02 Å but for which the standard deviation of that quantity over the $\pm$600 km s^{-1} window was such that $W_{r,lim}$ minus the standard deviation was less than or equal to 0.02 Å. This provision allows systems having a high variation in spectral quality across the absorption region to be included, and accounted for 6% of our final sample of 422 Mg II $\lambda\lambda$2796, 2803 doublets.

2.7. *Possible Sample Bias*

Since none of our quasar spectra were selected based upon knowledge of weak absorption, and because no correlation exists between strong and weak absorbers in a given quasar spectrum (Churchill et al. 1999), our sample is unbiased for weak systems. However, some of the spectra were selected because the presence of strong Mg II absorption had already been ascertained. Given this partial selection bias and the heterogeneous motivations behind the observations of some of these lines of sight, as discussed in § 2.1, it cannot be assumed *a priori* that the strong Mg II absorption subset is consistent with an unbiased sample. Some statistically significant reassurance of this would allow us to use our sample to study the evolutionary aspects of the strong Mg II absorption systems, which will be discussed in Paper II.

TABLE 2
STRONG Mg II W_r DISTRIBUTION EXPONENTIAL FIT RESULTS

Redshift Range	Data	N^*	W^* (Å)
$0.366 \leq z < 2.269$	this study	1.723 ± 0.178	0.810 ± 0.049
	Nestor et al. (2005)	1.187 ± 0.052	0.702 ± 0.017
$0.366 \leq z < 0.871$	this study	1.680 ± 0.032	0.829 ± 0.093
	Nestor et al. (2005)	1.216 ± 0.124	0.585 ± 0.024
$0.871 \leq z < 1.311$	this study	1.788 ± 0.035	0.667 ± 0.074
	Nestor et al. (2005)	1.171 ± 0.083	0.741 ± 0.032
$1.311 \leq z < 2.269$	this study	1.759 ± 0.307	0.922 ± 0.097
	Nestor et al. (2005)	1.267 ± 0.092	0.804 ± 0.034

In order determine whether our strong sample is not inconsistent with an unbiased one, the blind survey of 1331 Mg II absorbers of Nestor et al. (2005) was used for comparison. This comparison was touched upon in Evans et al. (2012) but we discuss it in more detail here. Their study measured Mg II λ2796 rest equivalent widths in the range $0.3 \leq W_r \leq 5.68$ Å and absorption redshifts $0.336 \leq z_{abs} \leq 2.269$. The maximum likelihood method was used to perform an exponential fit of the form $(\Phi/W^*)e^{-W/W^*}$ on the resulting distributions for both the entire sample and for three redshift bins, $0.336 \leq z < 0.871$, $0.871 \leq z < 1.311$, and $1.311 \leq z < 2.269$ (referred to in this section as the low, medium and high redshift samples). Φ is the normalization, W is the equivalent width, and W^* is the characteristic equivalent width. The Kolmogorov-Smirnov (KS) statistical test was employed in order to quantitatively measure the similarity (or lack thereof) between our sample of strong Mg II systems and the maximum likelihood exponential fits of Nestor et al. (2005).

Our equivalent width distributions are shown in Figure 5. They are plotted for both the entire redshift range and for the low, medium and high redshift samples. We have also performed maximum likelihood best fits on our unbinned equivalent width samples (e.g. Lanzetta et al. (1987)); these models along with those of Nestor et al. (2005) are shown with the data. The cumulative distributions are shown with the fits and KS test results in Figure 6. The maximum likelihood results are listed in Table 2.

Our criterion satisfying the assertion that our sample is not inconsistent with an unbiased sample was that $P(\mathrm{KS}) > 0.0027$, which would mean that it could not be ruled out at the 3 σ level that the two populations are consistent with one another. In all four redshift samples this criterion was met; for the full redshift range of Nestor et al. (2005), we obtained $P(\mathrm{KS}) = 0.115$, and for the low, medium and high redshift bins, we obtained $P(\mathrm{KS}) = 0.053$, 0.621, and 0.322, respectively. Even the lowest value, corresponding to the low redshift sample, falls well within the criterion, such that the two populations are not inconsistent with each other to even a 2 σ level. The exponential function maximum likelihood fit results for our sample and for those of Nestor et al. (2005) are also consistent within 3 σ of each other in all redshift bins.

Although our strong Mg II absorber sample is not inconsistent with an unbiased sample, Figure 5 reveals apparent excesses of absorbers at $W_r \simeq 2$ Å and $\gtrsim 4$ Å. These excesses are likely due to some of our quasar lines of sight being chosen for observation because the presence of DLAs was already known. This is primarily due to the HIRES spectra contributed by J. Prochaska, as well as some of the UVES spectra from the VLT archive. DLAs are associated with Mg II

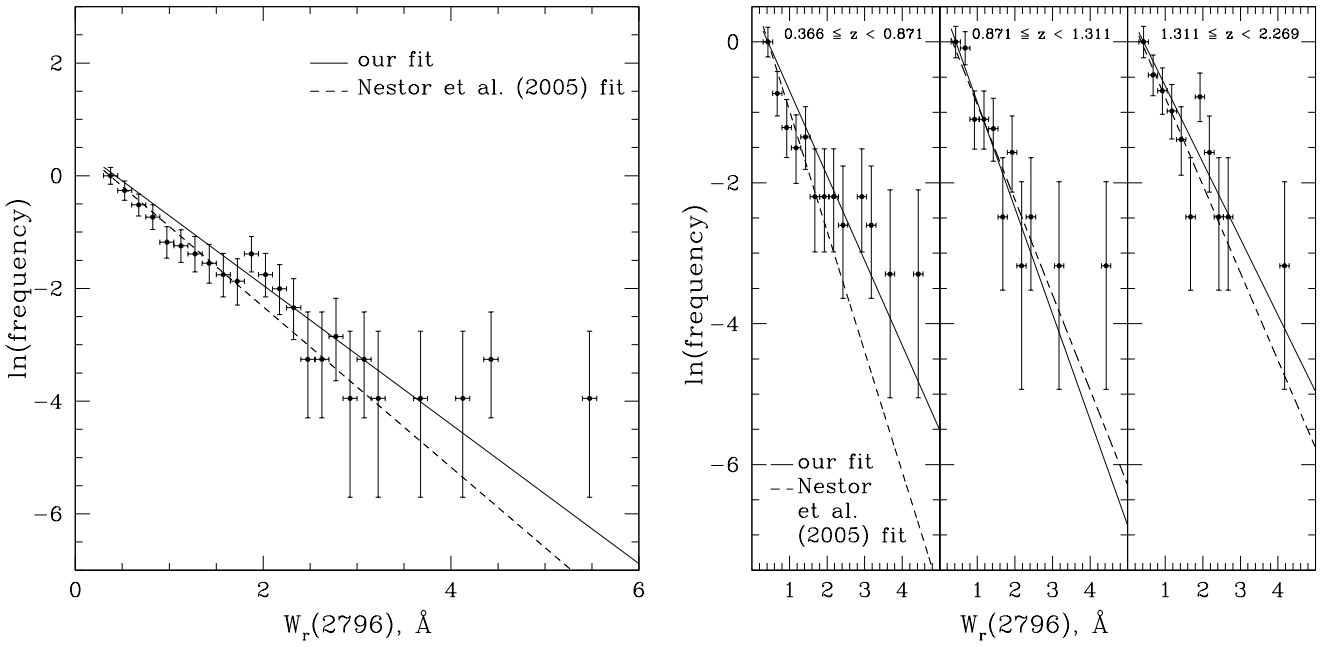

FIG. 5.— At left, the points show the Mg II λ2796 equivalent width distribution of our sample for $W_r \geq 0.3$ Å. The sloped lines indicate the maximum likelihood exponential fits to our sample (solid) and to the sample of Nestor et al. (2005) (dashed). At right, the same data is divided into the identical redshift bins of the sample of Nestor et al. (2005) and is plotted with the respective fits.

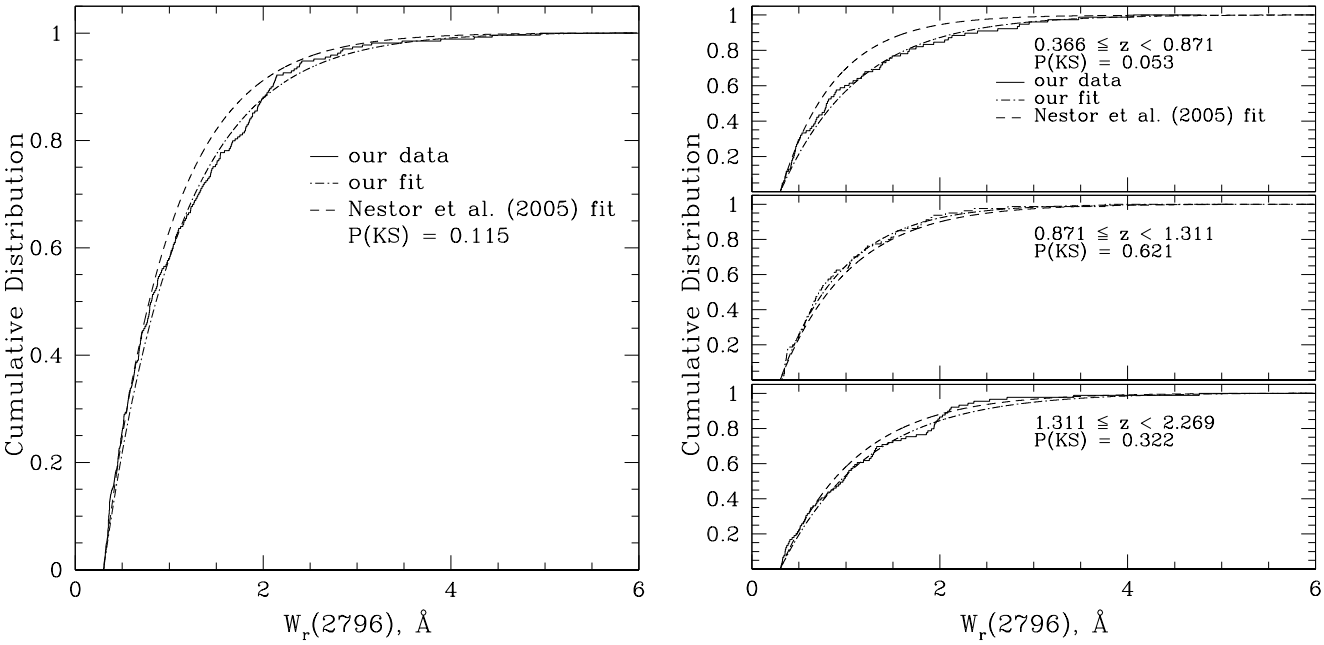

FIG. 6.— At left, the Mg II λ2796 cumulative equivalent width distribution of our sample (solid curve) for $W_r \geq 0.3$ Å and the maximum likelihood exponential fits to our sample (dashed-dotted curve) and to the sample of Nestor et al. (2005) (dashed curve). At right, the sample is divided into the identical redshift bins of the sample of Nestor et al. (2005) and is plotted with the respective fits. The P(KS) test results between our sample and the Nestor et al. (2005) fit are also noted.

absorbing systems in these equivalent width regimes. The excess at $W_r \gtrsim 4$ Å may also be indicative of galactic winds (see Bond et al. 2001a,b).

As a result of this analysis, we proceed under the premise that our sample of Mg II absorption systems has the characteristics of an unbiased sample, allowing the valid study of its evolution.

2.8. *Atomic Transitions and Example MgII Systems*

Although SEARCH locates numerous atomic transitions simultaneously when a Mg II λ2796 candidate is detected, measurements of the absorption features were limited to 13 transitions derived from five different elements: Mg II λ2796 and λ2803; Mg I λ2853; Fe II λ2344, λ2374, λ2383, λ2587, and λ2600; Ca II λ3935 and λ3970; and Mn II λ2577, λ2594, and λ2606. The transitions and their relevant atomic data are listed in Table 3. Column (1) lists the transition, (2) the vacuum wavelength, (3) the oscillator strength, and (4) the natural

TABLE 3
ANALYZED TRANSITIONS

Transition	λ_{vac} (Å)	f	Γ x 10^8 (sec^{-1})
Ca II3935	3934.777	0.6346	1.456
Ca II3970	3969.591	0.3145	1.414
Fe II2344	2344.214	0.1097	2.680
Fe II2374	2374.461	0.0282	2.990
Fe II2383	2382.765	0.3006	3.100
Fe II2587	2586.650	0.0646	2.720
Fe II2600	2600.173	0.2239	2.700
Mg I2853	2852.964	1.8100	4.950
Mg II2796	2796.352	0.6123	2.612
Mg II2803	2803.531	0.3054	2.592
Mn II2577	2576.877	0.3508	2.741
Mn II2594	2594.499	0.2710	2.685
Mn II2606	2606.462	0.1927	2.648

broadening constant.

Each system's absorption profiles for these transitions are shown in the online version of the Journal; six examples are shown in order of increasing equivalent width in Figures 7.1 and 7.2 with their VP models superimposed (Paper II will discuss this modeling).

3. RESULTS

Once the presence of Mg II is confirmed, the equivalent width regions, equivalent widths, optical depth-weighted system redshifts, velocity spreads, and upper and lower velocity limits are determined for both the whole system and for the kinematic subsystems using SYSANAL (see Churchill et al. 1999; Churchill & Vogt 2001). All quantities are calculated for the Mg II, Mg I, Fe II, Mn II, and Ca II transitions listed in Table 3.

The measured properties for example systems are listed in Table 4. Column (1) lists the quasar, (2) the system redshift, (3) the Mg II λ2796 rest equivalent width, (4) the apparent optical depth column density, (5) the Mg II $\lambda\lambda 2796, 2803$ doublet ratio, and (6) the flux decrement-weighted velocity spread, ω_v. The properties of example kinematic subsystems are listed in Table 5. Column (1) lists the quasar, (2) the system redshift, (3) the subsystem number, (4) the subsystem velocity center, $\langle v \rangle$, (5) the lower subsystem velocity limit, (6) the upper subsystem velocity limit, (7) the subsystem flux decrement-weighted velocity spread, ω_v, (8) the subsystem rest equivalent width for the Mg II λ2796 line, and (9) the subsystem Mg II $\lambda\lambda 2796, 2803$ doublet ratio. These properties are all derived directly from the flux values in each pixel and the methods of measuring them are discussed in the Appendix.

3.1. *Equivalent Width Distribution of* Mg II *Systems*

The system Mg II λ2796 equivalent width distributions of our low redshift ($0.19 \leq z < 1.4$) and high redshift ($1.4 \leq z \leq 2.55$) samples are shown in Figure 8. We fit exponential and Schechter functions to the binned data for both redshift ranges. The fits only included equivalent widths down to 0.032 Å (the bin centered on log $W_r = -1.375$ Å) due to the loss of sensitivity below this regime, which is discussed in § 2.3.

The exponential function takes the form $(\Phi/W^*)e^{-W/W^*}$, as discussed in § 2.7, while the Schechter function takes the form $\Phi(W/W^*)^{\alpha}e^{-W/W^*}$, where α is the faint end slope. The best fit parameter and reduced χ^2 results are shown in Table 6. The low redshift sample is clearly more well described by the Schechter function, with a reduced χ^2 of 4.43 versus 21.0 for the exponential fit. The Schechter result also produced a faint end slope of -0.463 ± 0.095, which is inconsistent with the zero value that would be implied by an exponential function.

In a study of H I mass densities traced by Mg II absorption, Kacprzak & Churchill (2011) fit a Schechter function to the equivalent width distribution of systems at $\langle z \rangle = 1.0$ and obtained best fit parameters of $W^* = 0.970 \pm 0.056$, which is slightly lower than our result of 1.043 ± 0.163, and $\alpha = -0.642 \pm 0.062$, slightly steeper than our result of -0.463 ± 0.095.

Comparing the exponential to the Schechter fits in the case of the high redshift sample, the reduced χ^2 values were 5.44 and 4.77, respectively; however, the best fit result for the faint end slope was -0.131 ± 0.161, which is consistent with zero and thus a simple exponential function.

Our low redshift equivalent width distribution is consistent with a Schechter function, which is comparable to a power law at the weak end. This is in broad agreement with the result of Churchill et al. (1999), who fit a power law to their weak $0.4 < z < 1.4$ distribution. However, Narayanan et al. (2007) found evidence for a turnover from a power law in their distribution within the same redshift range in that their weakest bin, 0.0165 Å $\leq W_r \leq$ 0.1 Å, fell significantly below the Churchill et al. (1999) fit.

Narayanan et al. (2007) also presented their weak equivalent width distribution for the range $1.4 < z < 2.4$ and compared it to their $0.4 < z < 1.4$ distribution. Though they did not perform fits to their distributions, they noted that qualitatively their low redshift weak distribution was the much steeper of the two. This is consistent with our results in comparing our high versus low redshift distributions.

It appears that the Mg II equivalent width distribution evolves over the total redshift range of $0.19 \leq z \leq 2.55$ from an exponential at high redshift into a Schechter at low redshift. The relative paucity of weak absorbers at high redshift may have been due to ionization conditions in the past that did not allow as many to survive. Another possibility that enrichment over time raises the Mg II column density of more H I clouds into a detectable range at low redshift.

Narayanan et al. (2007) speculated that the diminished number of weak Mg II absorbers above $z \sim 2$ might be due to the high redshift analogs of low redshift weak Mg II absorption being associated with strong Mg II. In this scenario, weak Mg II absorption at high redshift would be in the kinematic vicinity of strong Mg II and thus would not be recognized as isolated weak absorption. However, we have compared the high velocity weak kinematic subsystems of strong Mg II subsystems to isolated weak Mg II absorption (Evans 2011; Evans et al. 2012). Morphologically these two types of profiles often appear very similar, but a KS test of their rest equivalent width distributions revealed that they are actually two distinct populations to a 99.98% confidence level, or greater than 3 σ. A KS test of the distributions of flux decrement-weighted velocity spreads ω_v indicated to a greater than 6 σ confidence level that the two populations are unique.

3.2. *Kinematic Properties*

System total velocity width and velocity spread distributions are shown in Figure 9. The shaded histograms indicate the entire sample; the dotted lines indicate the weak ($W_r(2796) < 0.3$ Å) subsample; and the dashed lines indicate

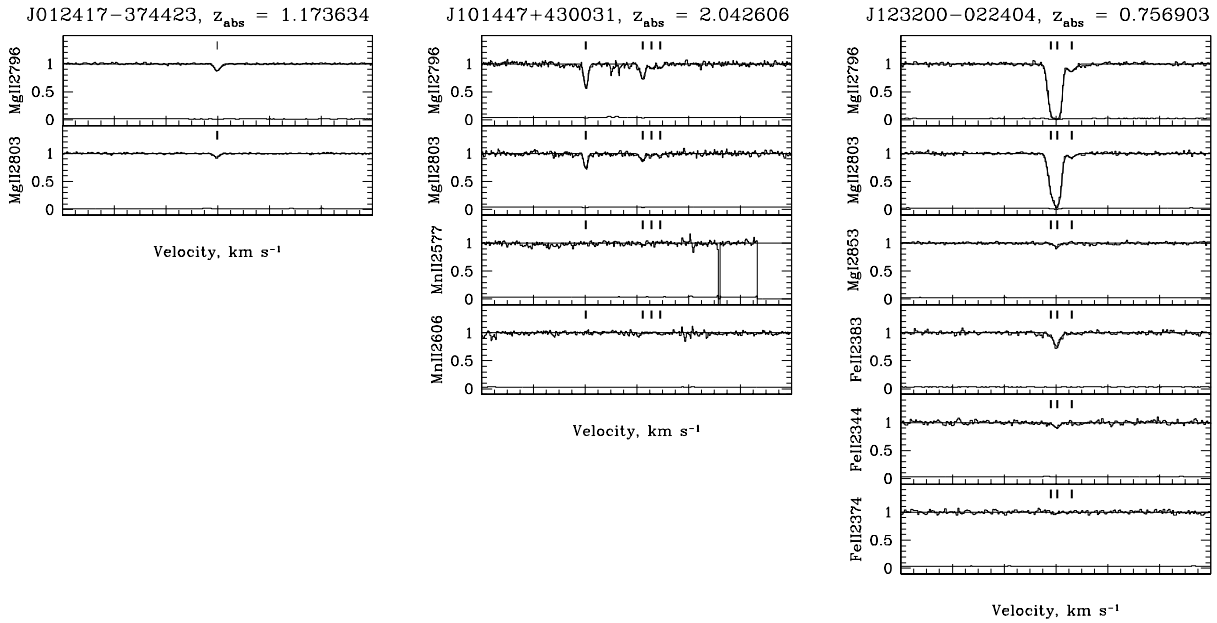

FIG. 7.1.— System absorption profiles. The VP models are superimposed; ticks indicate the component centroids.

TABLE 4
SYSTEM PROPERTIES

Quasar	z_{abs}	W_r (Å)	N_{aod} (log cm^{-2})	DR	ω_v (km s^{-1})
J012417−374423	1.173635	0.018 ± 0.001	$11.63^{+0.09}_{-0.07}$	1.84 ± 0.30	6.4 ± 1.0
J101447+430031	2.042606	0.092 ± 0.004	$12.39^{+0.05}_{-0.03}$	1.85 ± 0.17	59.6 ± 1.6
J123200−022404	0.756903	0.303 ± 0.003	$13.30^{+0.07}_{-0.06}$	1.28 ± 0.02	15.6 ± 0.7
J110325−264515	1.202831	0.593 ± 0.002	$13.44^{+0.04}_{-0.04}$	1.44 ± 0.01	43.3 ± 0.2
J110325−264515	1.838689	1.044 ± 0.001	$13.80^{+0.04}_{-0.03}$	1.33 ± 0.00	50.0 ± 0.1
J035405−272421	1.405188	2.660 ± 0.006	≥ 14.35	1.10 ± 0.00	93.3 ± 0.3

Notes. Results for the systems shown in Figures 7.1 and 7.2. Table 4 is published in its entirety in the electronic edition of the Journal. A portion is shown here for guidance regarding its form and content.

the strong ($W_r(2796) \geq 0.3$ Å) subsample. The two populations exhibit markedly different distributions, with the weak systems averaging a total velocity width of 88.7 km s^{-1} and the strong systems averaging 247.1 km s^{-1}. Similarly, the weak systems average a velocity spread of 22.9 km s^{-1} and the strong systems 60.0 km s^{-1}. The Mg II system total velocity width and velocity spread distributions indicate that differing kinematic extents, not just differing optical depths, contribute to the differences in equivalent widths in the weak and strong Mg II absorber populations.

The kinematic properties of Mg II absorbing systems can be further studied by quantifying characteristics of individual subsystems. We have divided the kinematic subsystems of the strong population (having total system $W_r(2796) \geq 0.3$ Å) into three classes according to subsystem velocity $\langle v \rangle$, choosing bins of $\langle v \rangle \leq 40$ km s^{-1}, $40 < \langle v \rangle \leq 165$ km s^{-1}, and $\langle v \rangle > 165$ km s^{-1}. This allows comparison with the work of Churchill & Vogt (2001), in which the subsystems of 23 strong Mg II systems were analyzed. Figure 10 shows the results of our analysis of the 242 strong systems in our sample. The left panel plots subsystem equivalent width versus subsystem velocity and the right panel subsystem velocity spread ω_v versus subsystem velocity; circles, x's and triangles represent the low, intermediate and high velocity bins, respectively.

The low velocity subsystems have an average equivalent width of 0.96 Å and an average velocity spread of 39.7 km s^{-1}. They represent a class distinct from the intermediate and high velocity subsystems, which have average equivalent widths of 0.29 and 0.20 Å, respectively, and average velocity spreads of 19.5 and 14.6 km s^{-1}, respectively. These data reflect the fact that low velocity subsystems tend to be the dominant subsystems in strong Mg II absorbers, whereas subsystems having $\langle v \rangle > 40$ km s^{-1} tend to be weak and to have smaller kinematic extents.

Our analysis of the kinematic subsystems of strong Mg II systems reveals that strong Mg II absorbers generally consist of a dominant subsystem with significantly weaker, kinematically more compact subsystems extending out in one or both directions from the main absorption and spaced tens to hundreds of km s^{-1} away.

Churchill & Vogt (2001) found the same trends between subsystem equivalent width and subsystem velocity and between subsystem velocity spread and subsystem velocity, namely, that lower velocity subsystems tend to exhibit both

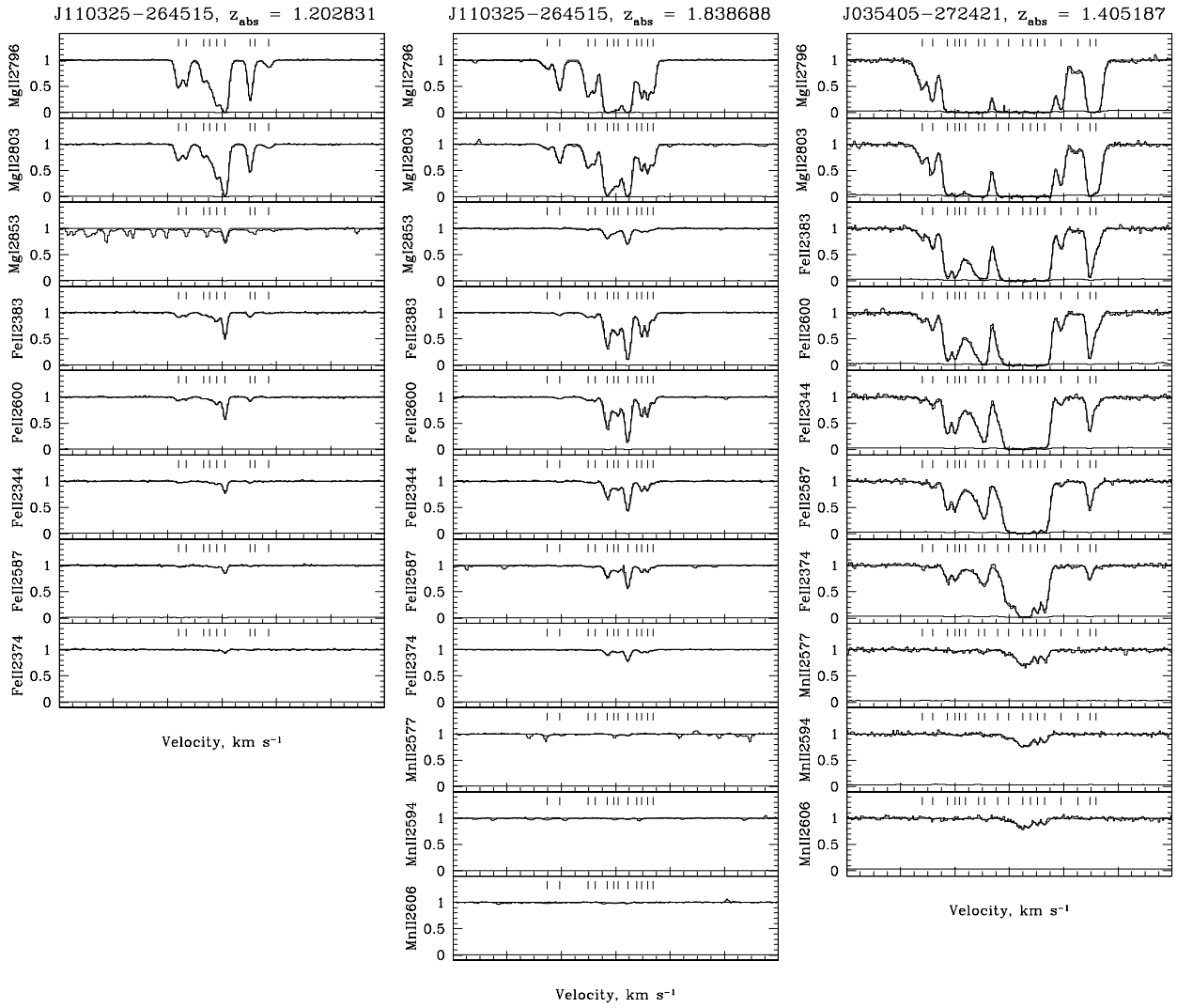

FIG. 7.2.— Same as Figure 7.1. Figures 7.1–7.422 are available in the online version of the Journal.

higher equivalent width and higher velocity spread than higher velocity subsystems. However, within each velocity bin, their subsystem velocity spreads and subsystem equivalent widths were significantly lower. In the low velocity bin, most of the subsystem equivalent widths ranged from $0.3 \leq W_r \leq 0.6$ Å compared to our average of 0.96 Å, and the velocity spreads were typically between $10 \leq \omega_v \leq 30$ km s^{-1} compared to our average of 39.7 km s^{-1}. Similarly, in the intermediate and high velocity bins, Churchill & Vogt (2001) found subsystem equivalent widths of $W_r \simeq 0.1$ Å whereas our average for those two bins is 0.25 Å. They also quote subsystem velocity spreads of typically < 10 km s^{-1} to our average of 17.5 km s^{-1}.

We believe these differences arise due to the much smaller sample size of Churchill & Vogt (2001) compared to our study; our sample is over a factor of ten larger. As a result, our sample includes the rarest extremely high equivalent width, high velocity spread Mg II systems, which are also more frequent in the higher redshift portion of our survey (Churchill & Vogt (2001) only covered up to $z = 1.2$). For example, the highest equivalent width system in the Churchill & Vogt (2001) sample had $W_r = 1.49$ Å, whereas for our sample it is $W_r = 6.23$ Å. The number of systems in our sample exceeding the Churchill & Vogt (2001) equivalent width maximum is 59, or 24% of the systems. We believe our sample is dramatically more robust and its statistics are the more reliable of the two.

3.3. *Evolution of Strong* Mg II *Systems*

In order to study evolution in strong Mg II absorbers, their flux decrements per pixel can be binned by absorption redshift, system equivalent width, and pixel velocity and the resulting cumulative distributions compared. This provides information about the relative system optical depths and the kinematic extents of the absorption and how these have changed through cosmic time.

The flux decrement in each pixel was measured in every equivalent width region in every Mg II system in our sample for the λ2796 feature. Pixels having decrements consistent with 1.0, i.e. saturated pixels, were assigned flux decrements of exactly 1.0, since their actual flux decrements vary about one due to noise. Pixels that were bad or that were part of a spurious feature, and thus had no corroborating absorption in other transitions, were omitted from the pixel sample.

TABLE 5
KINEMATIC SUBSYSTEM PROPERTIES

Quasar	z_{abs}	Subsystem	$\langle v \rangle$ (km s^{-1})	v^- (km s^{-1})	v^+ (km s^{-1})	ω_v (km s^{-1})	$W_r(2796)$ (Å)	DR
J012417−374423	1.173635	1	0.97 ± 0.86	−14.2	20.8	6.37 ± 1.04	0.02 ± 0.00	1.84 ± 0.30
J101447+430031	2.042606	1	-97.90 ± 0.48	−109.8	−81.7	4.88 ± 1.06	0.04 ± 0.00	1.71 ± 0.18
		2	19.67 ± 1.21	−4.1	53.7	13.74 ± 1.07	0.05 ± 0.00	2.01 ± 0.30
J123200−022404	0.756903	1	2.43 ± 0.41	−30.9	69.1	15.59 ± 0.67	0.30 ± 0.00	1.28 ± 0.02
J110325−264515	1.202831	1	-9.20 ± 0.22	−100.1	102.4	43.28 ± 0.21	0.59 ± 0.00	1.44 ± 0.01
J110325−264515	1.838689	1	-4.95 ± 0.11	−149.9	97.6	50.00 ± 0.12	1.04 ± 0.00	1.33 ± 0.00
J035405−272421	1.405188	1	-0.59 ± 0.33	−196.9	190.6	93.30 ± 0.29	2.66 ± 0.01	1.10 ± 0.00

Notes. Results for the systems shown in Figures 7.1 and 7.2. Table 5 is published in its entirety in the electronic edition of the Journal. A portion is shown here for guidance regarding its form and content.

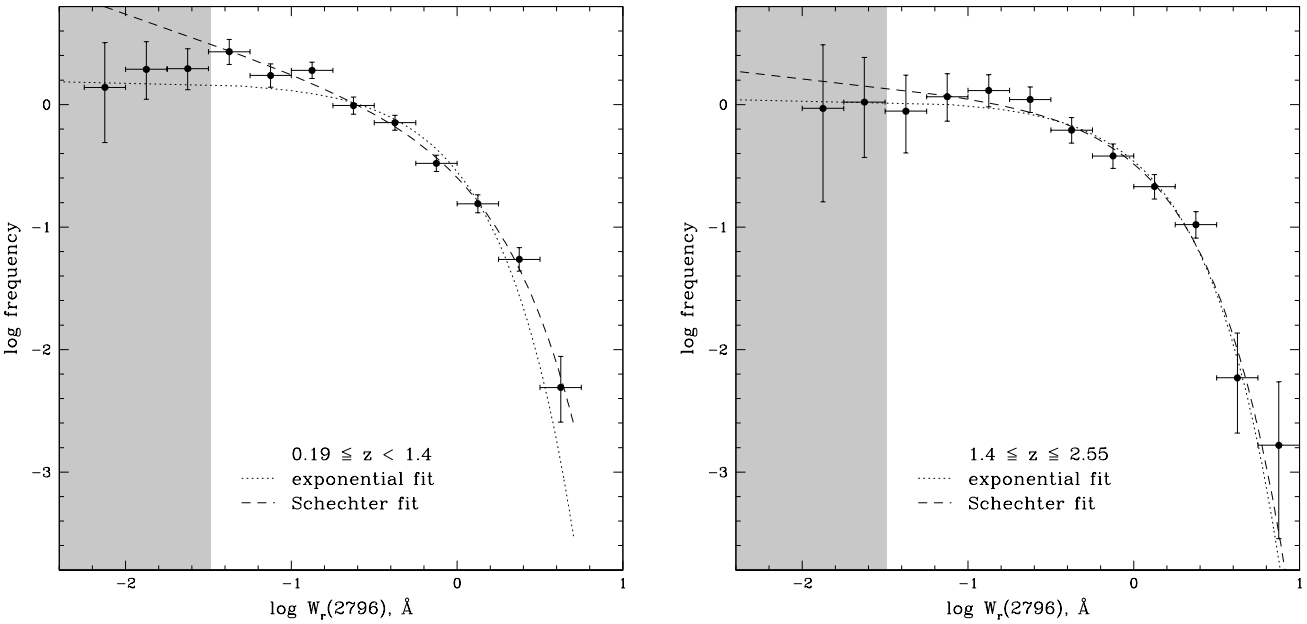

FIG. 8.— MgII λ2796 equivalent width distributions for our low redshift ($z < 1.4$, left) and high redshift ($z \geq 1.4$, right) samples. The dotted and dashed curves represent the best fit exponential and Schechter functions, respectively, and the best fit parameters are listed in Table 6. The fits do not include bins that fall within the shaded area, $W_r < 0.0325$ Å. This is the equivalent width regime in which our sample falls below 90% completeness (see § 2.3).

TABLE 6
W_r DISTRIBUTION FITTING RESULTS

z Range	Fit	Φ	W^* (Å)	α	χ^{2a}
low	1	1.545 ± 0.159	0.589 ± 0.046	···	21.0
low	2	0.648 ± 0.173	1.043 ± 0.163	-0.463 ± 0.095	4.43
high	1	1.096 ± 0.163	0.866 ± 0.094	···	5.44
high	2	0.915 ± 0.275	0.974 ± 0.190	-0.131 ± 0.161	4.77

[a] reduced

z Range. (low) $0.19 \leq z < 1.4$; (high) $1.4 \leq z \leq 2.55$.

Fit. (1) exponential; (2) Schechter.

We chose our absorption redshift binning, as in § 2.7, to match the redshift bins of Nestor et al. (2005). The pixels were binned according to $0.336 \leq z < 0.871$, $0.871 \leq z < 1.311$, and $1.311 \leq z < 2.269$ (hereafter the low, medium and high redshift samples). The pixels were further divided into equivalent width bins of $0.3 \leq W_r < 0.6$ Å, $0.6 \leq W_r < 1.0$ Å, $1.0 \leq W_r < 2.0$ Å, and $W_r \geq 2.0$ Å; this allows us to determine whether there is differential evolution based on absorption strength. Finally, the pixels were also binned according to their velocities to examine kinematic evolution with redshift. The method of measuring the relative pixel velocities is discussed in the Appendix.

The cumulative distributions of the resulting flux decrement samples are shown in Figures 11 - 12. Each panel plots the low, medium and high redshift distributions for a given equivalent width and velocity range.

The KS test was used to quantitatively compare the three distributions within each panel. In each case the test was performed on the low and medium redshift samples; the medium and high redshift samples; and the low and high redshift samples. This resulted in a P(KS) statistic, a measure of the equality of two samples, for each pair. The quantity $1-P$(KS) is the confidence level that the two samples are not drawn from the same population; the results are noted in each panel. Ellipses indicate that no data existed for the given redshift, equivalent width and velocity bin. For all panels for which $W_r \geq 2.0$ Å, we chose not to perform the KS test between the low and medium redshifts and between the medium and high redshifts because the medium redshift bin contained only four absorption systems. The medium redshift data for these panels is still shown, but we do not believe these distributions are as

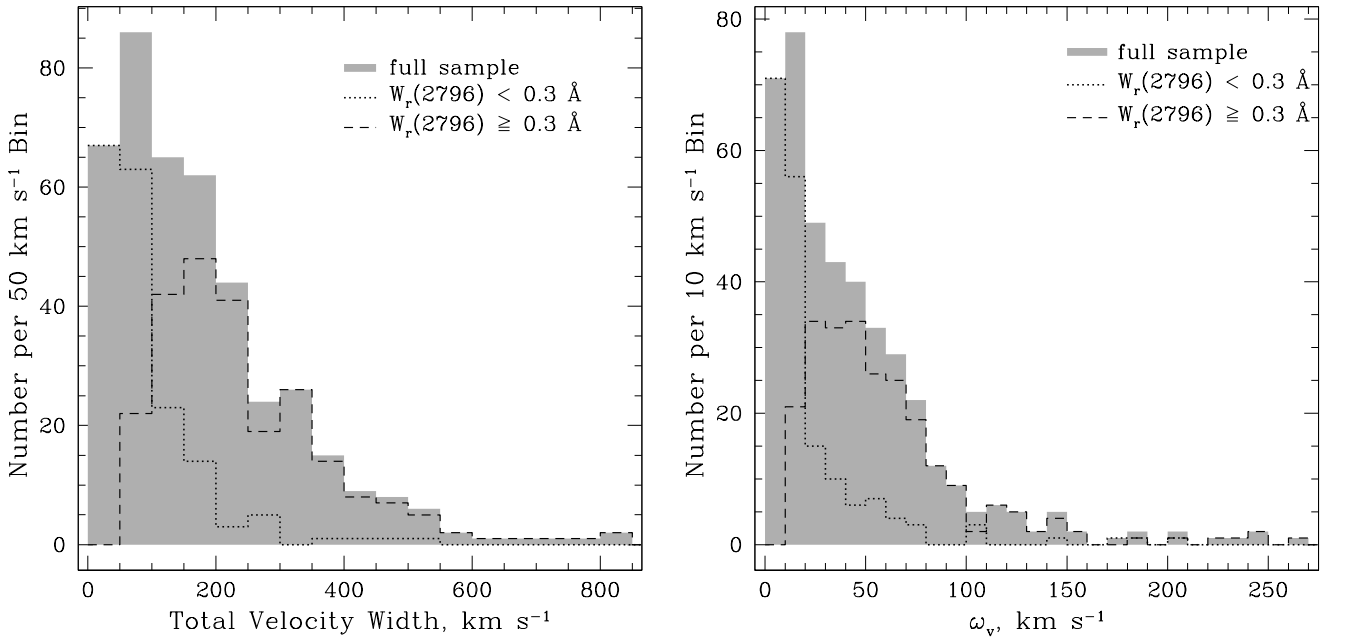

FIG. 9.— At left, the distributions of Mg II system total velocity widths for the λ2796 transition for $W_r(2796) < 0.3$ Å (dotted), $W_r(2796) \geq 0.3$ Å (dashed), and the full sample (solid gray). At right, the velocity spread (ω_v) distributions shown in the same format.

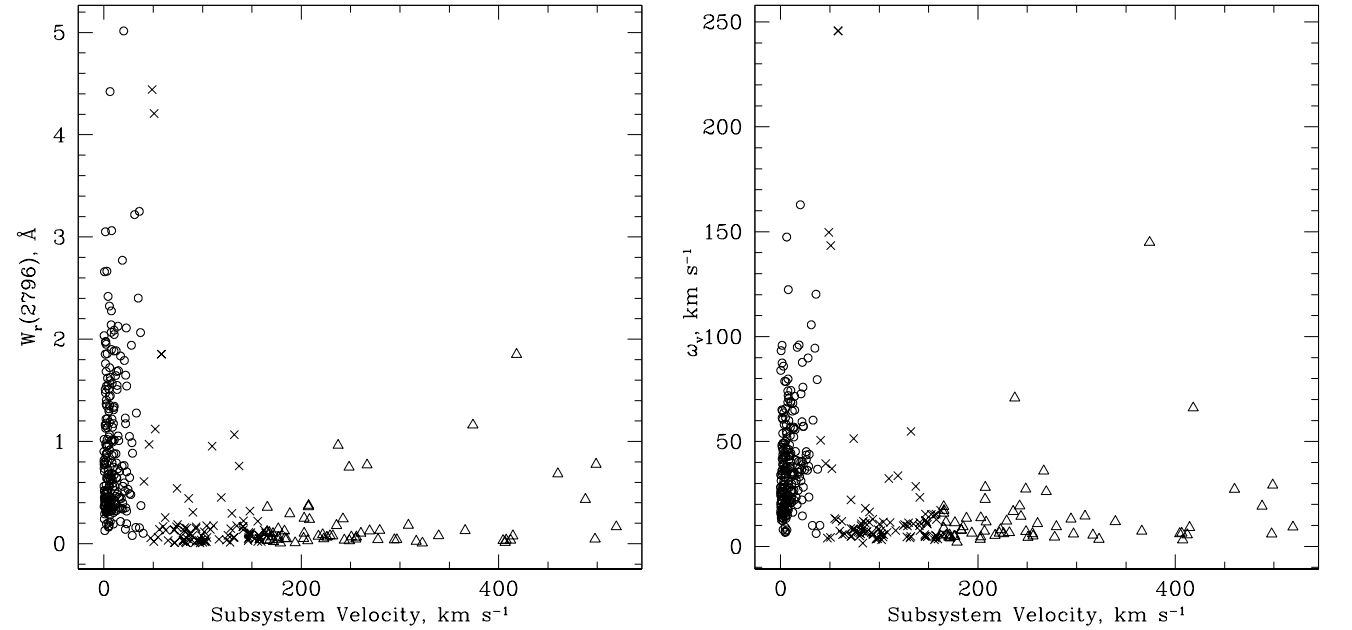

FIG. 10.— At left, subsystem equivalent width versus subsystem velocity for strong systems (total $W_r(2796) \geq 0.3$ Å). At right, subsystem velocity spread ω_v versus subsystem velocity for strong systems. Circles represent subsystem velocities $\langle v \rangle \leq 40$ km s^{-1}; x's $40 < \langle v \rangle \leq 165$ km s^{-1}; and triangles $\langle v \rangle > 165$ km s^{-1}.

robust as the others.

For this study we consider two samples to be statistically different if the confidence level resulting from the KS test exceeds 3 σ. For test results of less than 3 σ significance, the actual quantity $1-P$(KS) is noted; otherwise the confidence level is noted in terms of σ significance.

Figure 11 shows the flux decrement distributions, from top to bottom panels, over increasingly large velocity windows. The top row of the left panel includes only those pixels for which the velocity is within ± 50 km s^{-1}, the next row for which it is within ± 100 km s^{-1}, and so on. The distributions are plotted in this manner up to ± 450 km s^{-1}, and finally for the entire velocity window. In general these samples change less and less as the velocity window grows because most of the absorbing pixels are concentrated near the profile center. This is especially true of the $0.3 \leq W_r < 0.6$ Å sample, the lowest equivalent width bin.

In contrast, Figure 12 shows the flux decrement distributions, from top to bottom panels, over progressively smaller velocity ranges. Instead of plotting the distributions of pixels

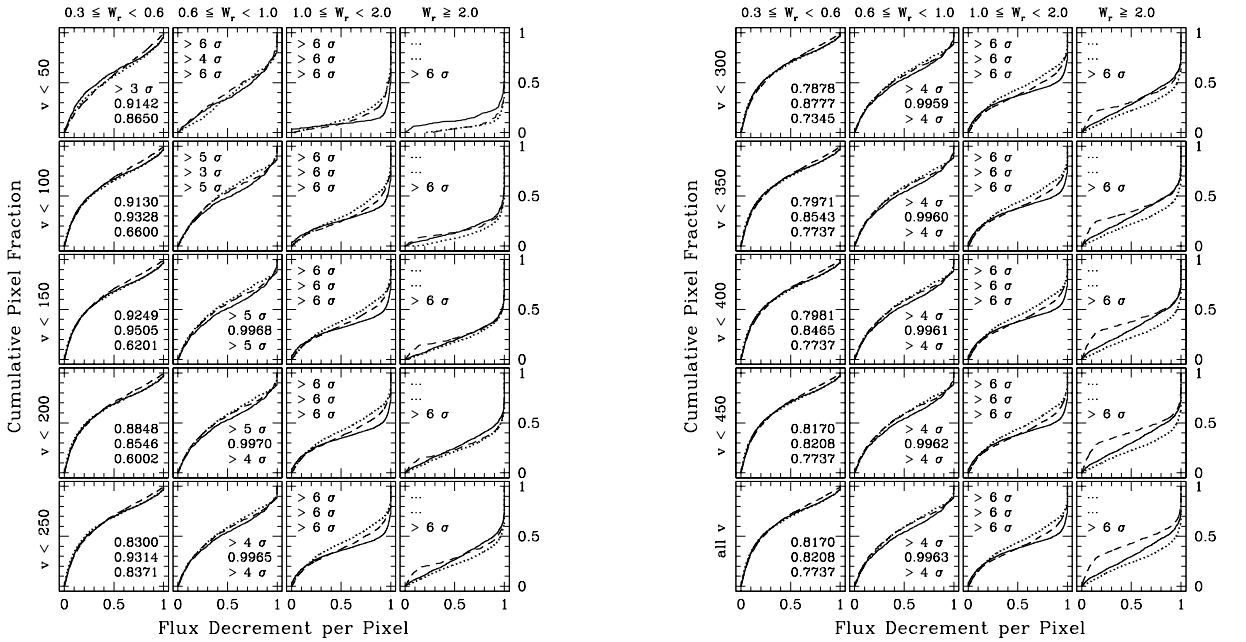

FIG. 11.— The Mg II λ2796 flux decrement per pixel distribution. The data is binned from left to right across panels by the rest equivalent width of the Mg II system in Å, and from top to bottom by the velocity range of the pixels in km s^{-1}. The solid, dashed and dotted lines trace the low, medium and high absorption redshifts, respectively; these bins are defined as $0.366 \leq z < 0.871$, $0.871 \leq z < 1.311$, and $1.311 \leq z < 2.269$. The confidence levels resulting from KS testing are shown from top to bottom in each panel for the low to medium redshift, medium to high redshift, and low to high redshift comparisons, respectively.

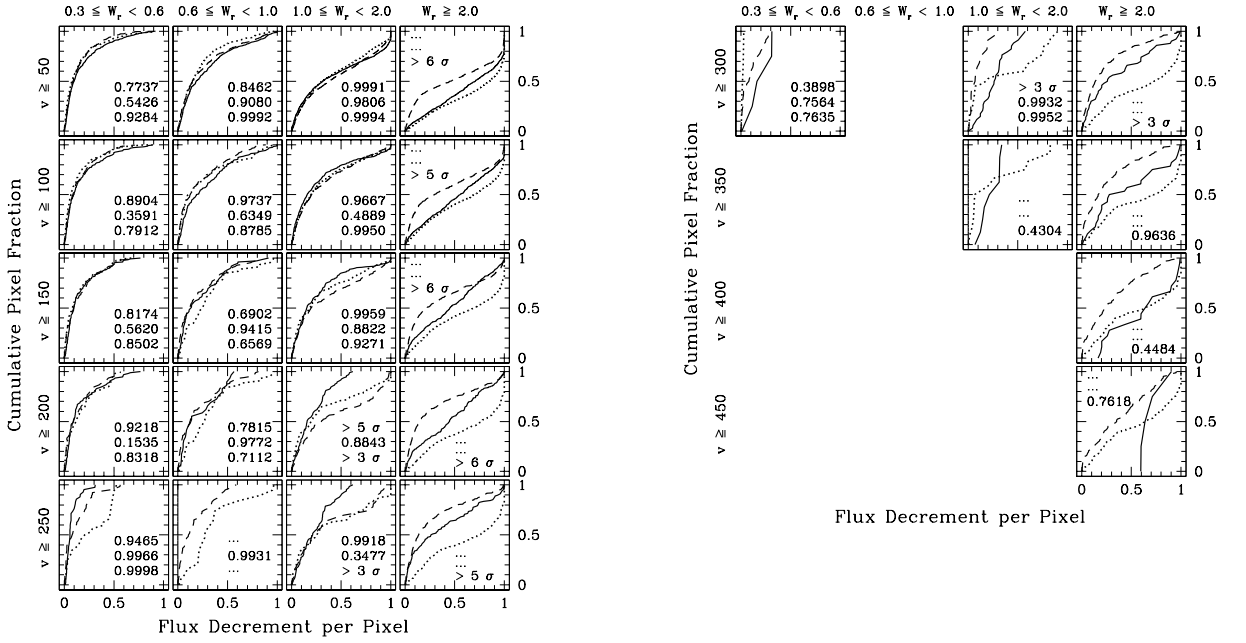

FIG. 12.— Same as in Figure 11.

in the central portions of the absorption profiles as in Figure 11, here we have plotted the distributions of pixels having velocities greater than some minimum velocity. The first row of the left panel includes only pixels for which the velocity is at least 50 km s^{-1} away from the zero point, the next row for which the velocity is at least 100 km s^{-1} away, and so on up to $v \geq 450$ km s^{-1}. In this velocity bin only the strongest systems, those having $W_r \geq 2.0$ Å, contain any absorption and therefore they were the only distributions shown. A number of panels in the $v \geq 300$ km s^{-1} or greater bins contained no absorbing pixels and were omitted. While Figure 11 shows the distribution of pixels within a given velocity, Figure 12 shows the distribution of pixels outside of a given velocity. Therefore distributions may not contain any pixels once the higher velocity cutoffs are reached, particularly in the lower equivalent width bins.

For the $0.3 \leq W_r < 0.6$ Å sample, there is for the most part no statistically significant evolution in the flux decrements ex-

cept in the case of low to medium redshift pixels having $v < 50$ km s^{-1}, in which case there is evolution at the 3 σ level. The low redshift distribution rises more steeply than the medium redshift, indicating that the low redshift systems tend to have weaker absorption within this velocity range than they do at medium redshift.

The next strongest sample, having equivalent widths of $0.6 \leq W_r < 1.0$ Å, contains statistically significant flux decrement evolution for all velocity ranges in Figure 11, i.e., the inner pixels of the absorption profiles. For $v < 50$ km s^{-1} and $v < 100$ km s^{-1}, these systems evolve between low and medium redshifts, between medium and high redshifts, and between low and high redshifts. Over larger velocity windows significant evolution occurs between the low and medium redshifts and between the low and high redshifts. The evolution is such that the medium redshift distribution rises the most steeply in the smallest velocity ($v < 50$ km s^{-1}) window, meaning it has the shallowest absorption of the three redshift bins in the profile cores; but in all larger velocity windows, the high redshift distributions rise the most steeply, implying that the absorption in any given pixel tends to be shallower than in the other two redshift bins. In contrast, the low redshift sample in this equivalent width range rises the most slowly. These profiles are as a group the most kinematically concentrated of the three.

These trends are continued in a more pronounced fashion in the next largest equivalent width range, $1.0 \leq W_r < 2.0$ Å. As expected, the flux decrement distributions of these stronger absorption systems rise more slowly than those of the weaker systems; this is due to the stronger profiles being more frequently saturated or nearly saturated over larger velocity ranges in all three redshift bins than the weaker profiles. Among the three redshift ranges in this equivalent width sample, evolution is found at the 6 σ level for all the inner velocity distributions. As noted for the $0.6 \leq W_r < 1.0$ Å sample, the low redshift distributions rise the least rapidly in all of these velocity windows, and the high redshift distributions the most rapidly, indicating that a greater proportion of the absorbing pixels in the former are strongly decremented than in the latter.

It is also in this equivalent width bin that we begin to see significant evolution in the outer pixels of the absorption profiles (Figure 12). In the range $v \geq 200$ km s^{-1} there is evolution between the low and medium redshift samples and between the low and high redshift samples at the 5 σ and 3 σ levels, respectively; in the range $v \geq 250$ km s^{-1} there is evolution between the low and high redshift samples at the 3 σ level; and in the range $v \geq 300$ km s^{-1} there is evolution between the low and medium redshift samples at the 3 σ level. At these high velocities there are fewer absorbing pixels in general; however, what pixels there are show a very different trend than those in the inner velocity distributions. The outer velocity distributions allow us to isolate and scrutinize absorption trends in the wings of the profiles. Here we see that the low redshift distributions in the higher velocity cutoff panels rise much more steeply than those of the medium and high redshifts, which tells us that in the outer portions of low redshift profiles, absorption in equivalent width regions is on the whole weaker per pixel.

For the strongest Mg II absorption bin, i.e. $W_r \geq 2.0$ Å, we have chosen to compare only the low and high redshift samples due to the small sample size of the medium redshift sample of only four systems. However, between the low and high redshift bins, as in the $1.0 \leq W_r < 2.0$ Å sample, there is strong evidence for evolution. In the inner velocity distributions, the high and low redshift distributions differ to a 6 σ significance level at all velocity cutoffs. The trend is for the low redshift distribution to rise more rapidly than that of the high redshift; this is due to the tendency of the low redshift profiles to have shallower absorption within a given velocity window than the high redshift profiles.

In these strongest systems there is also statistically significant evolution between the low and high redshift samples in all of the outer velocity distributions up to the $v \geq 300$ km s^{-1} bin; at greater velocity cutoffs there are not enough absorbing pixels to yield significant KS test results. As in the distributions for the outer velocity bins for the $1.0 \leq W_r < 2.0$ Å sample, in the strongest equivalent width regime we also see the low redshift distributions rising more steeply than the high redshift ones due to the pixels in the wings of the low redshift profiles containing, on average, weaker absorption than those in the high redshift profiles.

The studies of Steidel & Sargent (1992) and Nestor et al. (2005) concluded that the numbers per unit redshift dN/dz of $0.3 \leq W_r < 0.6$ Å systems are nonevolving. In higher equivalent width regimes, these authors found that evolution with redshift becomes increasingly significant (for $W_r \gtrsim 1.0$ Å and $W_r \gtrsim 2.0$ Å in the cases of Steidel & Sargent (1992) and Nestor et al. (2005), respectively). Their results regarding the numbers per unit redshift of strong systems indicated that the strongest systems diminish in number toward the present.

However, these studies were limited by their resolution in the types of analyses they could perform. Using our high resolution data, we measured flux decrements and kinematics as has never been done before for such a large sample and found that these quantities, like dN/dz, also evolve in very strong ($W_r \gtrsim 1.0$ Å) Mg II. This study complements the previous works, which could not investigate kinematics in any detail.

We find that systems having $W_r \geq 1.0$ Å exhibit the most marked changes in pixel flux decrements across our three redshift bins of $0.366 \leq z < 0.871$, $0.871 \leq z < 1.311$, and $1.311 \leq z < 2.269$. In general we find that statistically, the low velocity absorption (near the cores) of our strong Mg II profiles is stronger at lower redshifts, i.e. these regions are optically thicker than at high redshifts. In the higher velocity absorption regions, we find that on the whole the opposite is true; absorption per pixel is weaker at lower redshifts than at higher redshifts. These results indicate that high redshift Mg II absorbers in this equivalent width regime tend to have more kinematically extended absorption than do their low redshift counterparts.

Strong Mg II absorption is known to often, though not always, be associated with bright galaxies, and there are many instances of a specific galaxy being associated with a known Mg II system (see e.g. Kacprzak et al. 2008). In addition, it has been suggested that very strong ($W_r \geq 1.8$ Å) Mg II absorption often has kinematic structure suggestive of superwinds/superbubbles (Bond et al. 2001a,b). Zibetti et al. (2007), in a statistical study of stacked quasar field images, showed that strong Mg II absorption is correlated with significant light excesses within ~ 100 kpc impact parameters that are consistent with blue galaxies.

Earlier dN/dz studies have established definitively that the numbers of very strong Mg II systems are diminishing toward the present; for example, Nestor et al. (2005) find that $n(z)\sigma(z)$

of $W_r \geq 2.0$ Å systems decreases by $\sim 45\%$ from $z = 1.8$ to 0.6. However, it is apparent from our results that those very strong systems that do exist in the low redshift epoch contain more highly saturated profile centers, indicating that these structures are becoming more optically thick over time. This finding supports the suggestion of Steidel & Sargent (1992) that strong Mg II is optically thinner at high redshifts, as well as the conclusion by Nestor et al. (2005) that evolution they observe in the dN/dz of the very strong Mg II population must be driven by evolution in the kinematic properties of Mg II-selected galaxies.

Using the Spearman and Kendall rank correlation tests in our analysis of strong Mg II, we found no significant trend with redshift in the number of kinematic subsystems per system nor in the fraction of absorbing pixels (which may be less than one due to nonabsorbing pixels between subsystems). These findings contradict those of Mshar et al. (2007) who, in their study of 33 strong Mg II absorbers, stated that they observed significant correlation of these quantities with redshift. We stress that the kinematic evolution of strong Mg II is not easily characterized; in agreement with Mshar et al. (2007), we find that velocity spread also does not significantly evolve with redshift when the Spearman and Kendall rank correlation tests are employed. In addition, we have tested for evolution in total velocity width and VP Doppler *b* parameter distributions (the latter to be discussed in Paper II), also without finding significant differences in the populations at different redshifts.

It seems that the overall kinematic extents of very strong Mg II do not evolve, but that their internal velocity structure does. The optically thicker cores of the low redshift absorption profiles in our $W_r \geq 1.0$ Å subsample may indicate that the physical centers of the absorbing gas are becoming more settled over time. This would cause the flux removal to become more aligned and concentrated in velocity space. On the other hand, the trend we observe at greater velocities of increased kinematic complexity in the low redshift sample may indicate that the gas giving rise to the outer portions of the absorption is condensing into kinematically more distinct clumps.

4. DISCUSSION

Our Mg II equivalent width distribution is weighted more heavily toward weak systems at low redshift than at high redshift, an effect of both an increase in the incidence of weak absorbers (Narayanan et al. 2007; Evans et al. 2012) and a decrease in the incidence of very strong ($W_r \gtrsim 2$ Å) absorbers (Nestor et al. 2005; Lundgren et al. 2009) toward the present relative to the no-evolution expectation. Changes in ionization conditions could yield a higher weak dN/dz over time, while changes in kinematics, causing Mg II-selected gas to become more settled and thus aligned in velocity space, could reduce dN/dz of the strongest absorbers. The latter scenario is supported by the results our analysis of pixel flux decrements, which revealed significant kinematic evolution in the $W_r \geq 1.0$ Å population.

5. CONCLUSION

We searched 252 HIRES and UVES quasar spectra and identified 469 Mg II $\lambda\lambda 2796, 2803$ doublets in the range $0.1 < z < 2.6$ having $\langle z \rangle = 1.18$, of which 422 were included in the final sample after making the quality cut described in § 2.6. We classified 180 systems as weak (having $W_r < 0.3$ Å) and 242 as strong (having $W_r \geq 0.3$ Å). We analyzed each system's absorption and kinematic properties and modeled Voigt profiles.

1. The distribution of Mg II equivalent widths appears to evolve, being described by an exponential function at high redshift but by a Schechter function at low redshift. In the range $0.19 \leq z < 1.4$ we fit the distribution with a Schechter function having $\alpha = -0.463 \pm 0.095$ and $W^* = 1.043 \pm 0.163$. In the range $1.4 \leq z \leq 2.55$ we fit the distribution with an exponential function having $W^* = 0.866 \pm 0.094$.

2. Our weak absorbers averaged total velocity widths of 88.7 km s^{-1} and flux decrement-weighted velocity spreads of 22.9 km s^{-1}, while our strong absorbers averaged 247.1 km s^{-1} and 60.0 km s^{-1} for those two quantities, illustrating the relationship between absorber equivalent width and kinematic extent.

3. The kinematic subsystems of strong Mg II systems were segregated by velocity and their characteristics compared among velocity bins. The low velocity subsystems, having $\langle v \rangle \leq 40$ km s^{-1}, tend to be the dominant subsystems and to contain the majority of the system absorption; our low velocity subsystem sample has an average equivalent width of 0.96 Å and an average velocity spread of 39.7 km s^{-1}. The intermediate and high velocity subsystems, which have velocities of $40 < \langle v \rangle \leq 165$ km s^{-1} and $\langle v \rangle > 165$ km s^{-1}, average equivalent widths of 0.29 and 0.20 Å, and average velocity spreads of 19.5 and 14.6 km s^{-1}, respectively, representing relatively minor portions of the absorption in strong Mg II systems.

4. By studying the pixel flux decrement distributions of our strong Mg II sample, we found significant kinematic evolution among our low, medium, and high redshift subsamples ($0.366 \leq z < 0.871$, $0.871 \leq z < 1.311$, and $1.311 \leq z < 2.269$, respectively). The most pronounced kinematic evidence for evolution occurs in the $W_r \geq 1.0$ Å regime. The low redshift absorbers in this equivalent width range have systematically more strongly flux decremented pixels near the profile centers, and systematically shallower absorption in the outer portions of the profiles, than do their high redshift counterparts. The trend in the strong population is toward more kinematically concentrated gas over time.

We thank Wallace Sargent, Michael Rauch, Jason Prochaska, and Charles Steidel for their contribution of spectra. We are grateful for NSF grant AST 0708210, the primary funding for this work; JLE was also supported by a three-year Aerospace Cluster Fellowship administered by the Vice Provost of Research at New Mexico State University and by a two-year New Mexico Space Grant Graduate Research Fellowship. MTM thanks the Australian Research Council for a QEII Research Fellowship (DP0877998).

REFERENCES

Barlow, T. 2005, MAKEE software package, www2.keck.hawaii.edu/inst/hires/ data_reduction.html

Barton, E. J., & Cooke, J. 2009, AJ, 138, 1817

Bergeron, J., & Boissè, P. 1991, a, 243, 334
Bond, N. A., Churchill, C. W., Charlton, J. C., & Vogt. S. S. 2001, ApJ, 557, 761
Bond, N. A., Churchill, C. W., Charlton, J. C., & Vogt. S. S. 2001, ApJ, 562, 641
Chen, H.-W., Helsby, J. E., Gauthier, J.-R., Shectman, S. A., Thompson, I. B., & Tinker, J. L. 2010, ApJ, 714, 1521
Chen, H.-W., & Tinker, J. L. 2008, ApJ, 687, 745
Churchill, C. W. 1997, Ph.D. thesis, University of California, Santa Cruz
Churchill, C. W., Kacprzak, G. G., Nielsen, N. M., Steidel, C. C., & Murphy, M. T. 2012, ApJ, submitted
Churchill, C. W., Kacprzak, G. G., & Steidel, C. C. 2005, IAU Colloq. 199: Probing Galaxies through Quasar Absorption Lines, 24
Churchill, C. W., Rigby, J. R., Charlton, J. C., & Vogt, S. S. 1999, ApJS, 120, 51
Churchill, C. W., & Vogt, S. S. 2001, ApJ, 122, 679
Churchill, C. W., Vogt, S. S., & Charlton, J. C. 2003, ApJ, 125, 98
Dekker, H., D'Odorico, S., Kaufer, A., Delabre, B., & Kotzlowski, H. 2000, SPIE, 4008, 534
Evans, J. L. 2011, Ph.D. thesis, New Mexico State University
Evans, J. L., Churchill, C. W., Murphy, M. T. 2012, Nielsen, N. M., & Klimek, E. S., ApJ, submitted
Guillemin, P., & Bergeron, J. 1997, a, 328, 499
Kacprzak, G. G., & Churchill, C. W. 2011, ApJ, 743, 34
Kacprzak, G. G., Churchill, C. W., Evans, J. L., Murphy, M. T., & Steidel, C. C. 2011, MNRAS, 416, 3118
Kacprzak, G. G., Churchill, C. W., Steidel, C. C., & Murphy, M. T. 2008, AJ, 135, 922
Lanzetta, K. M., Turnshek, D. A., & Wolfe, A. M. 1987, ApJ, 332, 739
Lundgren, B. F., Brunner, R. J., York, D. G., Ross, A. J., Quashnock, J. M., Myers, A, D., Schneider, D. P., Al Sayyad, Y., & Bahcall, N. 2009, ApJ, 698, 819
Mshar, A. C., Charlton, J. C., Lynch, R. S., Churchill, C. W., Kim, T. 2007, ApJ, 669, 135
Murphy, M. T. 2008, UVES_popler software package, astronomy.swin.edu.au/ ∼mmurphy/UVES_popler
Narayanan, A., Misawa, T., Charlton, J. C., & Kim, T. 2007, ApJ, 660, 1093
Nestor, D. B., Turnshek, D. A., & Rao, S. M. 2005, ApJ, 628, 637
Nielsen, N. M., Churchill, C. W., & Kacprzak, G. G., ApJS, in preparation
Prochaska, J. X., Wolfe, A. M., Howk, J. C., Gawiser, E., Burles, S. M., & Cooke, J. 2007, ApJS, 171, 29
Rigby, J. R., Charlton, J. C., & Churchill, C. W. 2002, ApJ, 565, 743
Sargent, W. L. W., Steidel, C. C., & Boksenberg. A. 1988, ApJ, 334, 22
Schneider, D. P., et al. 1993, ApJS, 87, 45
Steidel, C. C., Dickinson, M., Meyer, D. M., Adelberger, K. L., & Sembach, K. R. 1997, ApJ, 480, 586
Steidel, C. C., Dickinson, M., & Persson, S. E. 1994, ApJ, 437, L75
Steidel, C. C., Kollmeier, J. A., Shapley, A. E., Churchill, C. W., Dickinson, M., & Pettini, M. 2002, ApJ, 570, 526
Steidel, C. C., & Sargent, W. L. W. 1992, ApJS, 80, 1
Veron-Cetty, M. P., & Veron, P. 2001, A&A, 374, 92
Weymann, R. J., Morris, S. L., Foltz, C. B., & Hewett, P. C. 1991, ApJ, 373, 23
Zibetti, S., Ménard, B., Nestor, D. B., Quider, A. M., Rao, S. M., Turnshek, D. A. 2007, ApJ, 658, 161

APPENDIX

Equivalent Width Regions

After a system is identified as described in § 2.4, its equivalent width region must be defined using the equivalent width spectrum and following the formalism of Schneider et al. (1993). The wavelength limits of the feature are determined by first measuring the equivalent width significance in each resolution element. There are three pixels per resolution element in our spectra and the instrumental spread function is assumed to be a Gaussian of width $\Delta\lambda$ (FWHM) given by $R = \lambda/\Delta\lambda = 45,000$. In order to have been identified, the feature must contain a resolution element satisfying the condition $w_j/\sigma_{w_j} \geq 5$, where w_j is the equivalent width of resolution element j and σ_{w_j} is the uncertainty in the equivalent width. From this resolution element the spectrum is then scanned blueward until the significance drops to $w_j/\sigma_{w_j} \leq 1$; this defines the lower wavelength limit of the spectrum. This process it repeated redward to locate the upper wavelength of the feature. An example of an identified system with the equivalent width regions defined for each kinematic subsystem is shown in Figure 14. The gray shaded areas indicate the equivalent width regions and the dotted lines indicate the limits of the 1 σ significance level.

Equivalent Widths

The equivalent width of an Mg II system results from both the column density of its components and its kinematics - i.e., the manner in which the components are distributed in velocity space. The rest frame equivalent width of an absorption line is equal to $W_r = W_{obs}/(1+z_{abs})$, where the definition of the observed equivalent width is

$$W_{obs} = \int_{\lambda_1}^{\lambda_2} \left(1 - \frac{I}{I^c}\right) d\lambda, \tag{1}$$

and where λ_1 and λ_2 are the wavelength limits of the feature, I is the flux at wavelength λ, and I^c is the continuum flux at that wavelength. In practice, the observed equivalent width of a system is determined by summing the equivalent width in each pixel over the wavelength range of the feature. For kinematic subsystem k spanning pixels j_k^- to j_k^+ the equivalent width is calculated as

$$W_k = \sum_{j=j_k^-}^{j_k^+} \left(1 - \frac{I_j}{I_j^c}\right) \Delta\lambda_j. \tag{2}$$

The quantity $D_j = 1-(I_j/I_j^c)$ is the flux decrement in pixel j and $\Delta\lambda_j$ is the wavelength range spanned by pixel j. The variance in W_k is

$$\sigma_{W_k}^2 = \sum_{j=j_k^-}^{j_k^+} \sigma_{D_j}^2 (\Delta\lambda_j)^2, \tag{3}$$

where $\sigma_{D_j}^2$ is the variance in the flux decrement and is given by

$$\sigma_{D_j}^2 = \left(\frac{I_j}{I_j^c}\right)^2 \left[\left(\frac{\sigma_{I_j}}{I_j}\right)^2 + \left(\frac{\sigma_{I_j^c}}{I_j^c}\right)^2\right], \tag{4}$$

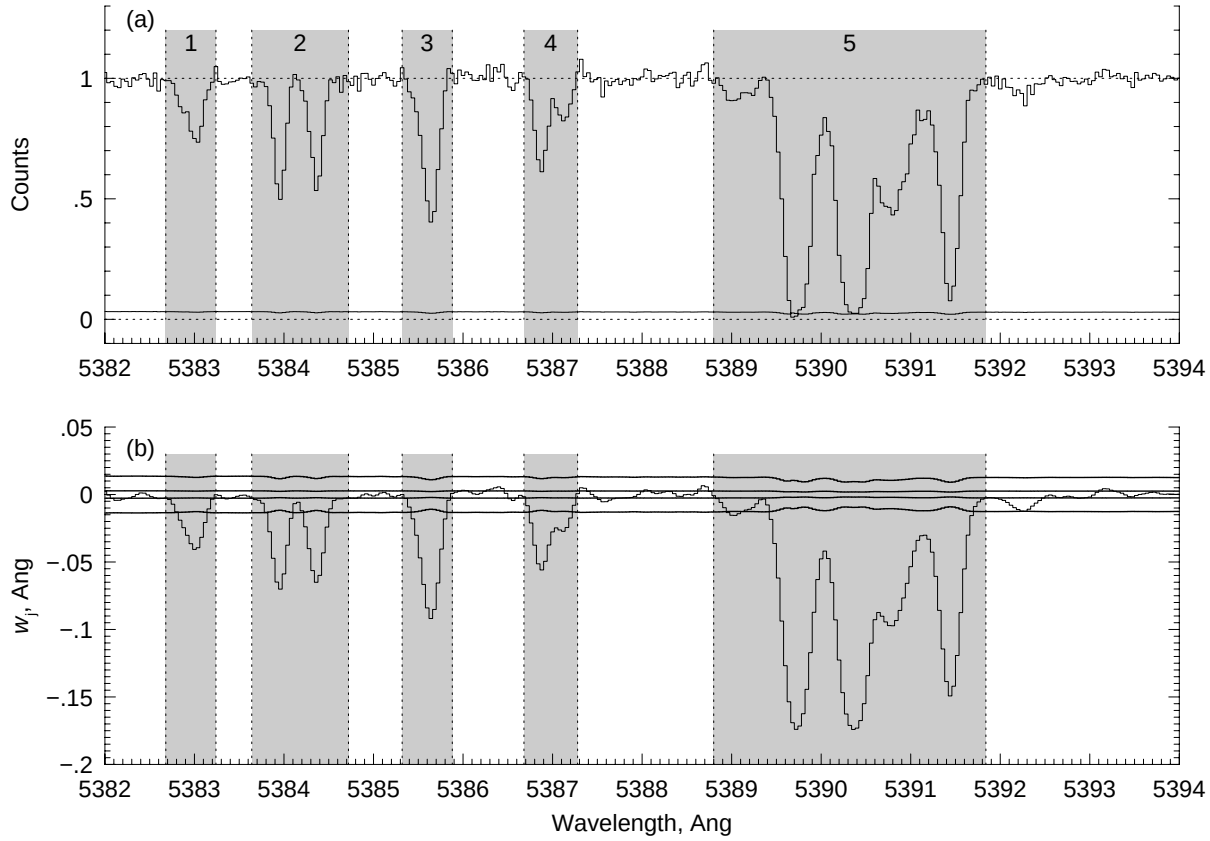

FIG. 14.— (a) Mg II λ2796 absorption system with its five kinematic subsystems defined. (b) The equivalent width per resolution element. The curves above and below the spectrum provide the $\pm 1\,\sigma$ and $\pm 5\,\sigma$ uncertainties. Figure provided by Churchill et al. (2012) with permission.

where σ_{I_j} and $\sigma_{I_j^c}$ are the uncertainties in the counts and continuum of pixel j.

The total system equivalent width then is summed over all subsystems as follows:

$$W = \sum_{k=1}^{N_{\rm sub}} W_k, \tag{5}$$

where $N_{\rm sub}$ is the number of kinematic subsystems. The variance for system equivalent width W is

$$\sigma_W^2 = \sum_{k=1}^{N_{\rm sub}} \sigma_{W_k}^2. \tag{6}$$

System Redshifts and Velocities

The system redshift is determined using the median wavelength of the flux decrement distribution of the Mg II λ2796 transition. This wavelength is obtained by solving the implicit equation

$$\int_{\lambda^-}^{\lambda_z} D(\lambda) d\lambda = \int_{\lambda_z}^{\lambda^+} D(\lambda) d\lambda \tag{7}$$

for λ_z. $D(\lambda)$ is the flux decrement at λ and λ^- and λ^+ are the lower and upper limits of the Mg II λ2796 absorption feature. The wavelength λ_z is then the spectral location at which there is an equal amount of integrated flux decrement blueward and redward. The system redshift is then calculated as $z_{abs} = [\lambda_z/\lambda_r(2796)] - 1$, where $\lambda_r(2796)$ is the rest wavelength of the Mg II λ2796 transition.

Once the system redshift has been determined, it can be used to transform the absorption profiles into velocity space. For a given observed wavelength λ_j of pixel j, the corresponding velocity is $v_j = c[\lambda_j - \lambda_r(1+z_{abs})]/[\lambda_r(1+z_{abs})]$, where c is the

speed of light and λ_r can refer to the rest wavelength of any of the transitions we are studying within the system. Converting the absorption profiles of all the selected system transitions into velocity space allows us to compare them on a common kinematic scale. In addition, we can now quantify and study kinematic properties.

Total Velocity Widths, Mean Velocities, and Velocity Spreads

The total velocity width of a system refers to the highest velocity v^+ of absorption minus the lowest velocity v^- of absorption in the Mg II λ2796 feature. This quantity represents the total velocity limits that a system spans, irrespective of the amount of absorption in the intervening velocity space. Thus a strong saturated profile spanning $\sim$ 600 km s^{-1} might have the same total velocity width as a weak system that has two kinematic subsystems, one at $\sim$ –300 km s^{-1} and the other at $\sim$ +300 km s^{-1} but with no absorption in between.

We can use the first three velocity moments to calculate the mean velocity $\langle v \rangle$ and the velocity spread ω_v of absorption systems and their subsystems. The definitions of the first three velocity moments are

$$V^{(0)} = \int_{v^-}^{v^+} D(v)dv, \quad V^{(1)} = \int_{v^-}^{v^+} vD(v)dv, \quad \text{and} \quad V^{(2)} = \int_{v^-}^{v^+} \left(v - \langle v \rangle\right)^2 D(v)dv, \tag{8}$$

where $D(v)$ is the flux decrement at velocity v.

The mean velocity or velocity center $\langle v_k \rangle$ of the kth kinematic subsystem is the ratio of the first to the zeroth moment:

$$\langle v_k \rangle = \frac{V_k^{(1)}}{V_k^{(0)}} \tag{9}$$

where the zeroth moment is calculated as

$$V_k^{(0)} = \sum_{j=j_k^-}^{j_k^+} D_j \Delta v_j, \tag{10}$$

and the first moment is

$$V_k^{(1)} = \sum_{j=j_k^-}^{j_k^+} v_j D_j \Delta v_j, \tag{11}$$

where Δv_j is the velocity width and D_j the flux decrement of pixel j.

The kinematic velocity spread, i.e. the dispersion of the flux decrement distribution, is given by

$$\omega_{v,k} = \left(\frac{V_k^{(2)}}{V_k^{(0)}} \right)^{1/2} \tag{12}$$

where the second velocity moment is calculated as

$$V_k^{(2)} = \sum_{j=j_k^-}^{j_k^+} (v_j - \langle v_k \rangle)^2 D_j \Delta v_j. \tag{13}$$

The variances in the mean velocity and velocity spread are given by

$$\sigma^2_{\langle v_k \rangle} = \left\{ \frac{\partial [V_k^{(1)}/V_k^{(0)}]}{\partial I_j} \right\}^2 \quad \text{and} \quad \sigma^2_{\omega_{v,k}} = \left\{ \frac{1}{2} \left[V_k^{(2)} \right]^{-1} \frac{\partial [V_k^{(2)}/V_k^{(0)}]}{\partial I_j} \right\}^2, \tag{14}$$

where

$$\left\{ \frac{\partial [V_k^{(n)}/V_k^{(0)}]}{\partial I} \right\}^2 = \sum_{j=j_k^-}^{j_k^+} \left\{ \frac{\left(V_k^{(0)} S_j^{(n)} - V_k^{(1)} S_j^{(0)} \right) \sigma_{D_j}}{\left[V_k^{(0)} \right]^2} \right\}^2, \tag{15}$$

$$S_j^{(0)} = -\frac{\Delta v_j}{I_j^c}, \quad S_j^{(1)} = v_j S_j^{(0)}, \quad \text{and} \quad S_j^{(2)} = (v_j - \langle v_k \rangle)^2 S_j^{(0)}. \tag{16}$$

As in the case of the equivalent widths, the total system velocity moments (denoted by dropping the subscript k) are obtained by summing over all subsystems:

$$V^{(0)} = \sum_{k=1}^{N_{\rm sub}} V_k^{(0)}, \quad V^{(1)} = \sum_{k=1}^{N_{\rm sub}} V_k^{(1)} \tag{17}$$

and the total system mean velocity is

$$\langle v \rangle = \frac{V^{(1)}}{V^{(0)}}. \tag{18}$$

The system second velocity moment is

$$V^{(2)} = \sum_{k=1}^{N_{\text{sub}}} \sum_{j=j_k^-}^{j_k^+} (v_j - \langle v \rangle)^2 D_j \Delta v_j \tag{19}$$

and the system velocity spread is

$$\omega_v = \left(\frac{V^{(2)}}{V^{(0)}} \right)^{1/2}. \tag{20}$$

The variances in the system mean velocity and velocity spread are

$$\sigma^2_{\langle v \rangle} = \left\{ \frac{\partial [V^{(1)}/V^{(0)}]}{\partial I_j} \right\}^2 \quad \text{and} \quad \sigma^2_{\omega_v} = \left\{ \frac{1}{2} \left[V^{(2)} \right]^{-1} \frac{\partial [V^{(2)}/V^{(0)}]}{\partial I_j} \right\}^2, \tag{21}$$

where

$$\left\{ \frac{\partial [V^{(n)}/V^{(0)}]}{\partial I} \right\}^2 = \sum_{k=1}^{N_{\text{sub}}} \sum_{j=j_k^-}^{j_k^+} \left\{ \frac{\left(V^{(0)} S_j^{(n)} - V^{(1)} S_j^{(0)} \right) \sigma_{D_j}}{\left[V^{(0)} \right]^2} \right\}^2, \tag{22}$$

$$S_j^{(0)} = -\frac{\Delta v_j}{I_j^c}, \quad S_j^{(1)} = v_j S_j^{(0)}, \quad \text{and} \quad S_j^{(2)} = (v_j - \langle v \rangle)^2 S_j^{(0)}. \tag{23}$$